CHEMISTRY OF MATERIALS

pubs.acs.org/cm

Article

Open Access

This article is licensed under CC-BY 4.0

Dimensionality Reduction Expands the Frontiers of Lanthanide Luminescence Thermometry Beyond Single-Parametric Thermal Sensing

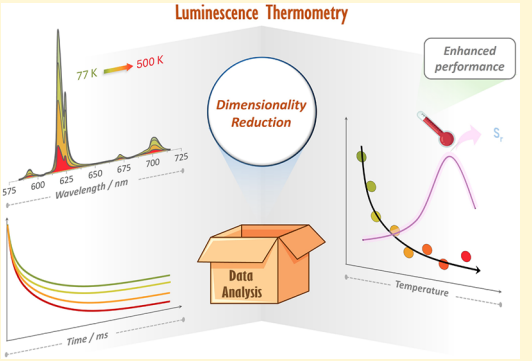
Leonardo F. Saraiva, Airton G. Bispo-Jr.,* André L. Costa, Fernando A. Sigoli,* Sergio A. M. Lima, and Ana M. Pires*

Cite This: *Chem. Mater.* 2025, 37, 3125−3136

Read Online

ACCESS | Metrics & More | Article Recommendations | Supporting Information

ABSTRACT: Luminescent thermometers (LThs) are particularly suitable for monitoring submicron-scale thermal changes, spurring substantial advances in the field. Compared with the efforts to maximize the performance of LThs by designing novel materials, few advances have been made at the methodological level to exploit classical thermometric essays. Such a viewpoint motivated this study, which sought to combine data analysis algorithms with multiple thermometric parameters to introduce an advanced perspective on postprocessing data methodologies. Specifically, three distinct dimensionality reduction (DR) algorithms were employed: multiple linear regression (MLR), non-negative matrix factorization (NMF), and kernel principal component analysis (k-PCA). These methods were applied to the proof-of-concept SrY_2O_4:$Tb^{III/IV}$,Eu^{III} phosphor using the thermal dependence of the thermally coupled levels of Eu^{III} (Δ) and the $^5D_0$ lifetime (τ). Compared to traditional fitting and integration analyses, the DR approach provided enhanced thermometric performance, achieving a sensitivity increase from 0.897% K^{-1} (using Δ) to 3.68% K^{-1} (using k-PCA) and reducing temperature uncertainty below 0.03 K (k-PCA). By moving beyond single parametric thermal sensing with DR, these outcomes enable us to push the limits of luminescence thermometry toward unexplored pathways.



INTRODUCTION

What we observe is not nature itself, but nature exposed to our methods of questioning. Werner Heisenberg, one of humankind's most important scientists, drafted these words in one of his books.[1] This quote elegantly underscores a foundation of scientific inquiry: our methods and tools shape the reality we observe. One physical property that exemplifies this concept is temperature, as the accuracy and reliability of the measurements depend on the techniques employed.[2] Among the currently available techniques, remote temperature measurement methods have emerged over the years to probe temperature in various environments. Yet, the time-response of a thermometer is constrained by its size,[3] which may hamper real-time measurements at the submicron level.[4] In this context, luminescence thermometry arose as one prominent approach to measuring temperature remotely by ensuring improved spatial and temporal resolution compared to their macroscopic competitors.[5,6]

Luminescence thermometry relies on harnessing temperature-induced changes in the optical properties of probes.[7] These variations are monitored remotely by acquiring a thermal readout of the environment in which the probe is in contact. Despite their young age, luminescent thermometers (LThs) have become compelling tools for biological and materials science research. As has been recently reported, they offer the potential to measure intracellular temperature,[8−10] and temperature during chemical reactions.[11−13] The strong appeal of this technology has resulted in a booming number of LThs over the years, and as with any continually evolving sphere of knowledge, questions about the applicability of LThs started to appear.[14] For instance, in the biological field,[15] researchers have addressed queries about biocompatibility and erroneous readouts caused by photon attenuation in biological tissues.[8−10,16] Questions on the sensitivity and/or errors during thermal readouts were also raised, prompting researchers to develop novel thermometers with improved performance,[17−21] Consequently, while new luminescent probes are being developed daily, advances at the methodological level are scarce.

Received: November 15, 2024
Revised: April 9, 2025
Accepted: April 10, 2025
Published: April 16, 2025



© 2025 The Authors. Published by American Chemical Society

Downloaded from pubs.acs.org/cmatex/article-pdf/37/9/3125/4187176/cm4c03173.pdf by UNIV ESTADUAL PAULISTA user on 05 November 2026

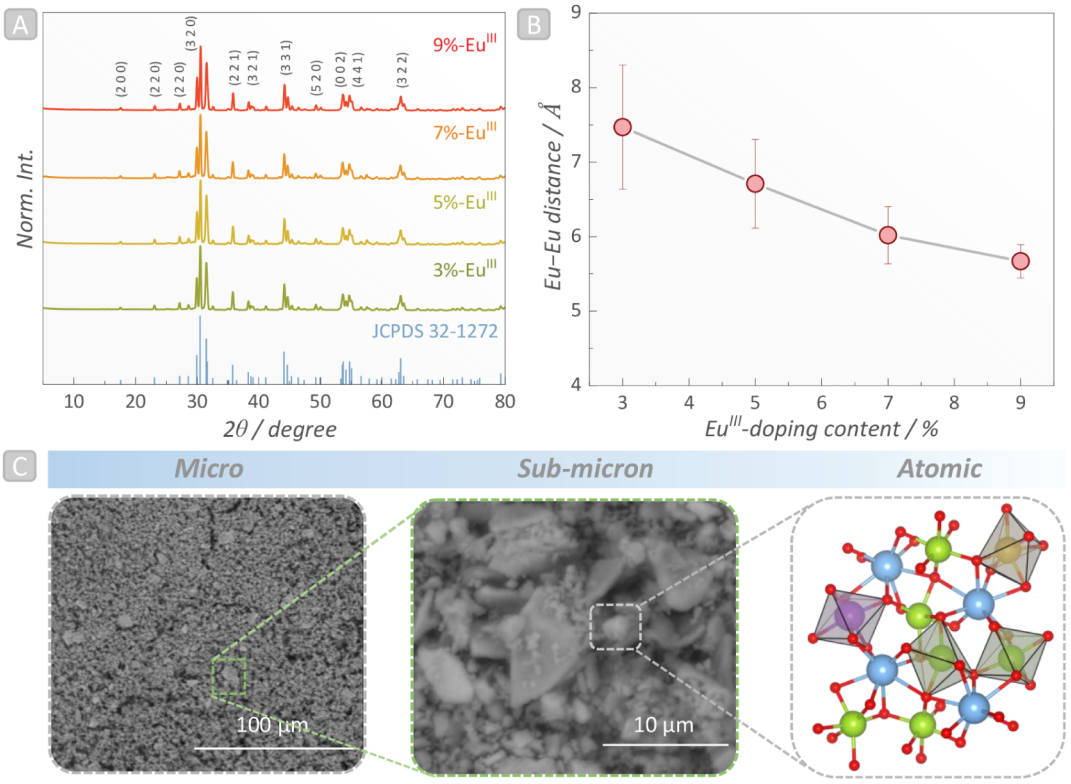


Figure 1. (a) Structural characterization of the SrY_2O_4:$Tb^{III/IV}$(2 at.%),Eu^{III}(3,5,7,9 at.%) phosphors by powder X-ray diffraction (PXRD). (b) Distribution curve of Eu^{III}–Eu^{III} distances using the Monte Carlo simulation method. (c) Scanning electron microscopy of the 5 at.%Eu phosphor, highlighting the micro, submicron, and atomic scales. The atomic representation was obtained from Rietveld refinement. The color code is as follows: blue = strontium, green = yttrium, orange = terbium, purple = europium, and red = oxygen.

The scarcity of advancements in postprocessing data methodologies is not confined to luminescence thermometry; indeed, guidelines for treating spectroscopic data are still a hot topic.[22−24] In luminescence thermometry, this difficulty arises from the trial-and-error approach, which is typically used to select the parameter most sensitive to temperature fluctuations. Given the range of parameters available—such as lifetime, emission ratio, and spectral shift[25,26]—the criterion for selecting a specific property remains unclear. Seeking to enlighten this problem, a handful of works integrating data analysis methods with luminescence thermometry have garnered attention.[27−30] Most of these studies employed multiple linear regression (MLR) on parameters with linear thermal dependence.[27,29] Despite this progress, the decision-making process for selecting and/or merging thermometric parameters is still heavily reliant on human judgment. Consequently, methodologies that minimize the human component are attractive for analyzing thermometric data. The use of machine learning (ML) and dimensionality reduction (DR) techniques holds a strong appeal for this purpose, and few studies have explored this area.[31−34]

Dimensionality reduction excels at handling large volumes of data, a common scenario in most thermometric essays. In essence, DR transforms data from a high-dimensional space into a low-dimensional space, retaining most of the relevant information.[35] Although DR methods may initially seem abstract, they are commonly applied to noise reduction, and voice recognition.[36] By translating this concept to the domain of LThs, a high-dimensional space would consist of the intensity vs several wavelengths and/or time at different temperatures, as pointed out by Ximendes et al.[31] Then, DR enables capturing hidden numerical quantities that correlate more effectively with temperature.

The use of DR algorithms in luminescence thermometry was pioneered by the work of Ximendes, Marin and coworkers.[31] In this study, the authors included the thermal dependence of the emission bands of $LiYF_4$:Nd^{III} nanoparticles and Ag_2S semiconductor nanocrystals (SNCs). Their approach rendered highly accurate LThs featuring high thermal resolution. However, the employed regression model based on principal component analysis (PCA) fully addressed only linearly dependent variables. The inclusion of the *t*-distributed stochastic neighbor embedding (*t*-SNE) method resolved this issue. Still, as highlighted by the authors,[31] the projection of data into reduced space using t-SNE was not straightforward. Furthermore, the PCA components crossed the zero boundary for the Ag_2S SNCs, making the evaluation of S_r rather difficult. These observations regarding DR raise an important caveat: *different algorithms yield distinct results for a single data set.*

These exciting works combining ML and/or DR methods demonstrated that data analysis algorithms not only enhance thermal sensitivity but also reduce uncertainties in temperature measurements. These procedures represent a remarkable advancement in the field by scratching only the surface of data analysis algorithms for luminescence thermometry. Yet, they rely on a single parameter, such as the ratio between two different emission bands. This prompts the question of whether combining multiple parameters with these algorithms can further improve the performance of LThs. Investigating this hypothesis may explore the avenues opened by these studies to unforeseen pathways to harness the full potential of different LThs.

https://doi.org/10.1021/acs.chemmater.4c03173
Chem. Mater. 2025, 37, 3125−3136

Downloaded from pubs.acs.org/cmatex/article-pdf/37/9/3125/4118176/cm4c03173.pdf by UNIV ESTADUAL PAULISTA user on 05 November 2026

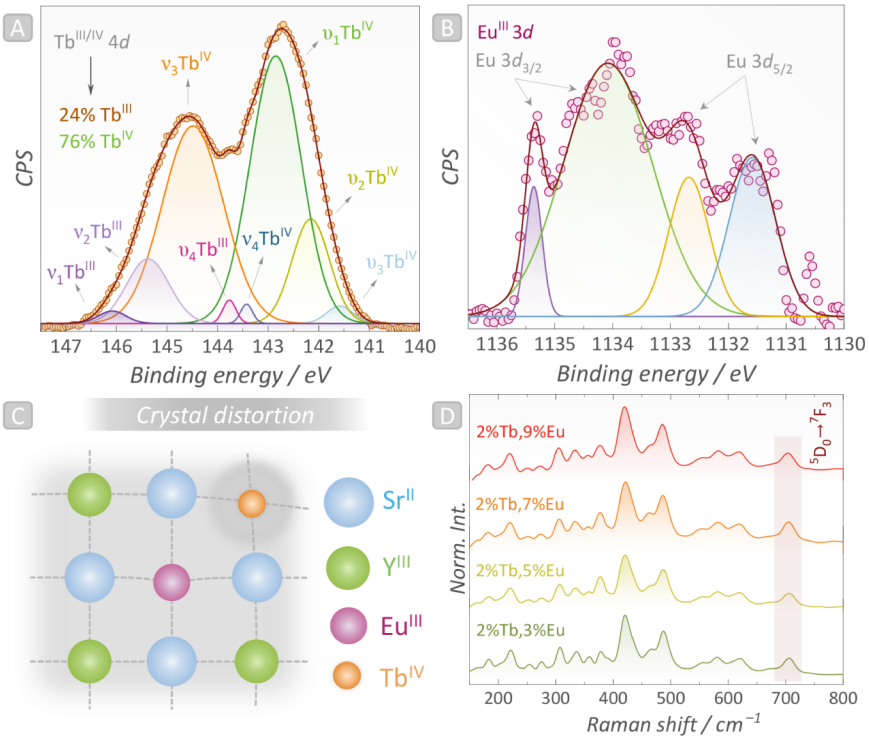


Figure 2. High resolution X-ray photoelectron spectra of SrY_2O_4:$Tb^{III/IV}$(2 at.%),Eu^{III}(5 at.%) focusing on (a) $Tb^{III/IV}$, where a 76% Tb^{IV} to 24% Tb^{III} proportion was obtained. (b) Eu^{III} 3*d* multiplets detected by XPS. (c) Representative scheme of lattice distortion caused by the presence of dopants. (d) Raman spectra of all samples using the 633 nm laser (2.0 mW). The band in 700 cm^{-1} observed in the Raman spectra is assigned to the $^5D_0 \rightarrow {}^7F_3$ Eu^{III} electronic transition.

Motivated by the numerous opportunities afforded by data analysis in luminescence thermometry and inspired by these pioneering works in the field, this study endeavors to demonstrate how a more general DR approach capable of addressing linear and nonlinear temperature dependencies can finely tune the performance of LThs. To substantiate this goal, the SrY_2O_4:$Tb^{III/IV}$,Eu^{III} phosphor was used as a proof-of-concept. Previous studies have shown that the use of quadruply oxidized lanthanides in SrY_2O_4:Eu^{III} phosphors increases the distance between adjacent Eu^{III} ions,[37] underlining the choice of this system. This effect is desirable when using the ratio between the Eu^{III} $^5D_1$ and $^5D_0$ emission bands (i.e, thermally coupled levels),[38] since the $^5D_1$ emission can be quenched by Eu^{III}–Eu^{III} energy migration. Furthermore, it is well-known that the Eu^{III} $^5D_0$ population is highly reliant on temperature, thereby aiding the use of the lifetime's thermal dependence as a secondary thermometric parameter, yielding a dual-parametric approach. Aware of this interplay, the kernel-PCA algorithm was chosen as the primary DR method to lead the analysis of dual-parametric thermometry. Its choice was driven by its ability to capture both linear and complex nonlinear relationships, unlike traditional PCA (a formal definition can be found in Notes S1 and S2).[39] For sake of comparison, we also employed MLR and non-negative matrix factorization (NMF) to evaluate the performance gains of different DR methods. The harnessed outcomes enable advancing post-processing data methodologies in luminescence thermometry while optimizing luminescent thermal probes to experimentally achievable thresholds.

RESULTS AND DISCUSSION

Phosphor Selection and Characterization. The general procedure for synthesizing the phosphor has been reported by us elsewhere, in which an adaptation of the conventional Pechini method was used.[37] The detailed synthetic procedure and characterization apparatus are described in the Methods. The photophysical response of compounds is highly reliant on their structural parameters. Therefore, to optimize the conditions for higher $^5D_1$ and $^5D_0$ emissions, the $Tb^{III/IV}$ concentration was fixed at 2 at.%, while the Eu^{III} content was varied from 3 to 9 at.% in odd-number increments. Powder X-ray diffraction (PXRD) measurements confirmed the successful accomplishment of the phase of interest, where all peaks were indexed to SrY_2O_4 (JCPDS 32-1272), Figure 1a. The Rietveld analysis (Figures S1–S4 and Table S1) revealed that increasing the Eu^{III} doping content led to an expansion of the lattice, as indicated by Table S3. However, the replacement of Y^{III} sites by Tb^{IV} resulted in a lower volume of unit cell for the 9 at.%-Eu^{III} sample compared to the 7 at.%-Eu^{III}. When this replacement occurs, the Y^{III} sites become less available for substitution, forcing Eu^{III} to increase their replacement at Sr^{II} sites.

Gaining further comprehension of the interaction between adjacent Eu^{III} ions is crucial, which can be achieved by observing the Eu^{III} distribution within the phosphor. This understanding was garnered by Monte Carlo simulations (Note S2—Ln–Ln distances), providing a mean Eu^{III}–Eu^{III} distance within the host. The 3 at.%-Eu^{III} displays a 7.47 Å Eu^{III}–Eu^{III} distance, while the 9 at.%-Eu^{III} sample had a separation of 5.78 Å. Such outcome confirms quantitatively the intuitive obviousness that higher Eu^{III} concentrations decrease the mean Eu^{III}–Eu^{III} distance (Figure 1b). Although these

Downloaded from pubs.acs.org/cmatex/article-pdf/37/9/3125/4118176/cm4c03173.pdf by UNIV ESTADUAL PAULISTA user on 05 November 2026

https://doi.org/10.1021/acs.chemmater.4c03173
Chem. Mater. 2025, 37, 3125–3136

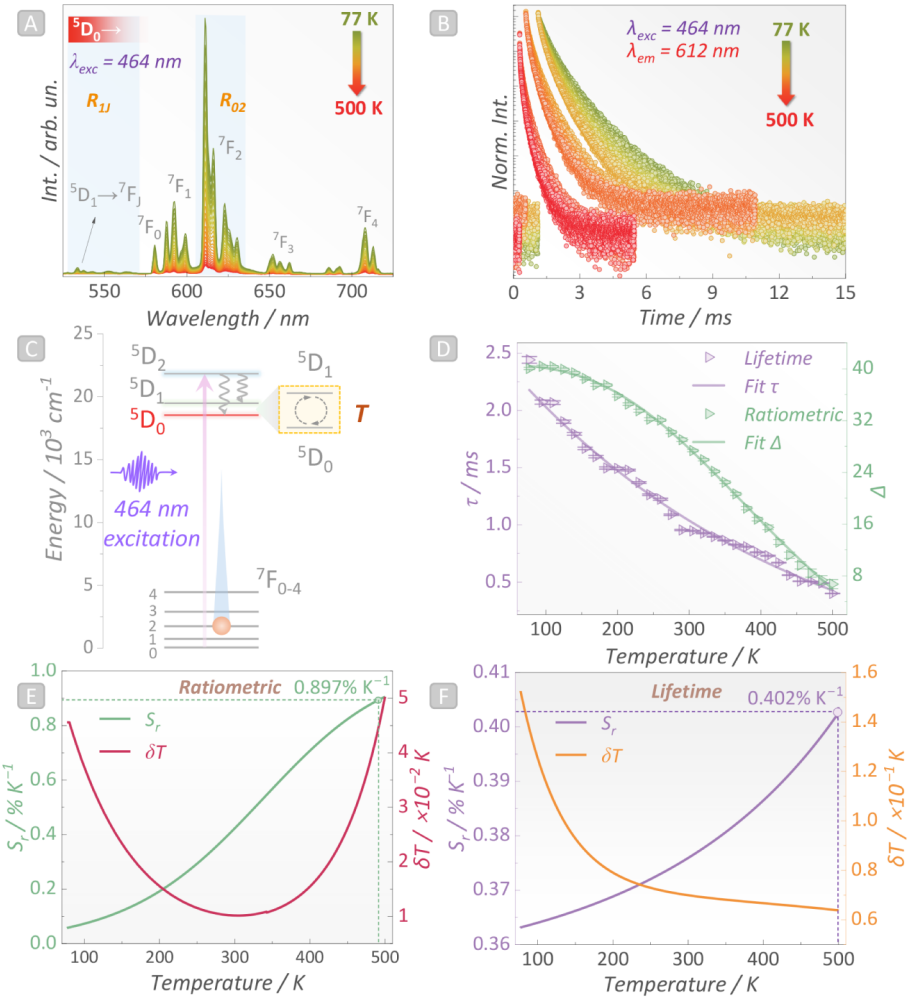


Figure 3. (a) Temperature dependent (77−500 K) emission spectra undertaken upon 464 nm excitation, highlighting the $^5D_0$ and $^5D_1$ emission bands (Figure S14). (b) Temperature-dependent lifetime of the $^5D_0$ level within the same temperature range. (c) Partial energy diagram showing the excitation on the $^5D_2$ manifold, $^5D_{0,1}$ thermally coupled levels, and emission arising from the $^5D_0$ state. (d) Temperature-dependent thermometric parameter (Δ) calculated from the intensity ratio between $^5D_0$ and $^5D_1$ emission bands or the $^5D_0$ level lifetime. Relative thermal sensitivity (S_r) and temperature uncertainty (δT) dependence considering (e) the ratiometric or (f) lifetime approaches.

variations may seem significant, they are only reasonable compared to the referenced works.[40−43] This implies that Eu^{III} replaces multiple sites within the crystal structure, suggesting an organized distribution.

Focusing on one of the phosphors is a natural step toward more comprehensive analysis. In this context, scanning electron microscopy (SEM) revealed a heterogeneous distribution of particles for the 5 at.%-Eu^{III} phosphor (Figures 1c and S5). This distribution is characteristic of Pechini synthesis, where this route yields nanostructured materials with agglomerations.[37] Despite this behavior, the chemical mapping performed by energy dispersive spectroscopy (EDS) revealed a homogeneous distribution of aggregates of Eu^{III} ions within the phosphor (Figures S6 and S7). Concurrently, these aggregates were sparser for $Tb^{III/IV}$ ions, implying a more uniform distribution.

The presence of Tb in the phosphor was verified by chemical mapping (Figure S7). However, the question of how it can influence the optical features of the phosphor remains to be answered since Tb^{III} emits in the green spectral region, whereas Tb^{IV} is spectroscopically inert. X-ray photoelectron spectroscopy (XPS) analysis revealed a composition of 24% Tb^{III} and 76% Tb^{IV} (Figure 2a). It is important to note that the reduction of rare-earths (RE) by X-rays is a well-known effect[44,45] and cannot be neglected, implying that the actual amount of Tb^{IV} could be even greater than 76%. The complete assignment of the XPS peaks is summarized in Table S4, Figures S8 and S9. Additionally, Eu^{III} peaks were detected, which can be attributed to the $3d_{5/2}$ and $3d_{3/2}$ multiplets, further confirming the successful doping of Eu^{III} (Figure 2b), which induced the significant crystal distortion seen in the Rietveld analysis (Figure 2c). Such effects have been heavily studied to increase the emission of lanthanide-based compounds, since symmetrical environments with an inversion center forbid the forced-electric dipole mechanism, which is responsible for 4*f* transitions.[46]

When aiming to not only enhance but also study the luminescence of a compound, attention is drawn toward its vibrational structure, as vibrational quenching can suppress luminescence. In this context, Raman spectroscopy is often used to probe phonon energies, and the measured spectra of all samples are depicted in Figure 2d. Under undoped conditions, the SrY_2O_4 matrix possess 12 Sr and Y sites in the unit cell, leading to 28 Raman-active modes with distinct irreducible

https://doi.org/10.1021/acs.chemmater.4c03173
Chem. Mater. 2025, 37, 3125−3136

Downloaded from pubs.acs.org/cmatex/article-pdf/37/9/3125/4187176/cm4c03173.pdf by UNIV ESTADUAL PAULISTA user on 05 November 2026

representations,[37] of which 13 were observed (Figure S10 and Table S5). These vibrational modes are merely combinations of stretching, bending, and wagging within the crystal structure.[47] The remaining 15 modes may overlap, contributing to the broad baseline observed in the spectra (Figure 2d). A closer inspection of the Raman spectra enabled us to determine the mean phonon energy ($\hbar\bar{\omega}$), which was extracted by the deconvolution of the most energetic vibrations in the Raman spectra (Figure S11). The mean values were 584.2, 586.3, 584.1, and 584.8 cm^{-1} for the 3, 5, 7, and 9 at.%-Eu^{III} samples, respectively. Notably, as expected, the variation in the phonon energies was feeble, implying that Eu^{III}-doping had little impact on this feature. These small variations are attached to changes in the RE−O bond lengths, which are assigned to lattice distortions and the induction of defects within the crystal structure.

Taking the 5 at.%-Eu^{III} sample as a reference, since it displayed the most distinct mean phonon energy, simulations on this property were performed (Figure S12); for further detail of the methodology, proceed to Note S2—phonon calculations. At the Γ-point, i.e., the center of the Brillouin zone, a maximum vibration of 565 cm^{-1} was observed, exhibiting a 3.7% relative deviation from the experimental value. This error may be attached to the fact that Raman scattering does not probe true Γ-point phonons. During scattering, a finite momentum $\boldsymbol{q}$ is added due to momentum conservation, which is determined by geometry and crystal orientation.[48] Such a phenomenon implies the need to consider the phonon dispersion along the path of high-symmetry points (Figure S12).[49,50] Overall, the lattice distortion caused by dopants holds significant impact in changing the distance between Eu^{III} ions, whereas the mean phonon energies are almost unaffected, allowing for the parametrization of the mean energy.

Conventional Luminescence Thermometry and Emission Dynamics. After harvesting the structural insights, examining the luminescent properties of the phosphors becomes a logical next step. In this context, all phosphors exhibit the characteristic set of Eu^{III} emission bands in the red spectral region, which are assigned to the $^5D_0 \rightarrow {}^7F_{0-4}$ transitions (Figure S13) under 464 nm ($^5D_2 \leftarrow {}^7F_0$) excitation. It should be mentioned that this excitation channel was selected to further mitigate any Tb^{III} emission despite its low amount in the sample. In this context, the emission bands in the 524−565 nm region were attributed to the $^5D_1 \rightarrow {}^7F_{0-2}$ electronic transitions, which were detected due to the reasonably low mean phonon energy of the phosphor. The thermometric study was conducted on the 5 at.%-Eu^{III} sample, which was carefully chosen because of its highest relative emission intensity among the phosphors (Figure S13b). This behavior can be attached to the relatively low mean Eu^{III}−Eu^{III} distances in the 7 at.% and 9 at.%-Eu^{III} samples, which allows a more efficient energy migration between the Eu^{III} ions.

The thermal response of the emission and the average $^5D_0$ lifetime calculated from a biexponential function (eq S6) for the selected phosphor is summarized in Figure 3, covering the 77−500 K temperature range. As expected, there is a drastic decrease in the emission intensity with increasing temperature, accompanied by a corresponding decrease in the $^5D_0$ level lifetime. It is worth highlighting briefly that in lifetime measurements with time-correlated single photon counting (TCSPC) devices, special attention should be paid to the time range in which the decay curve is monitored.[24] The lifetime reduction at increased temperatures may cause the necessity to reduce the time range to avoid baseline errors, as seen in Figure 3b; otherwise, this potentially leads to an incorrect fitting. The emission and lifetime thermal dependences are directly related to the population of the $^5D_0$ state, as a reduction in the population leads to a lower intensity and shorter lifetime (Figure 3a,b). In the presence of thermally coupled levels, such phenomena occur due to the thermal population of higher excited manifolds ($^5D_1$, for instance, which features an energy gap of ≈1700 cm^{-1}). However, as seen in Figure S14, the emission intensity of the $^5D_1$ bands also decreased, indicating unusual non-Boltzmann behavior. This behavior has been observed and rationalized by Geitenbeek *et al.*,[38] however, the underlying reasons for this phenomenon were addressed only qualitatively. Providing a quantitative analysis of this behavior is nontrivial, as distinct mechanisms may compete. Among these possibilities, cross-relaxation (CR) and multiphonon relaxation (MPR) are highlighted (Figure S15). In the CR process, the $^5D_1$ level may be deactivated according to the relation: $\{^5D_1 \rightarrow {}^5D_0\} \leftrightarrow \{^7F_0 \rightarrow {}^7F_3\}$. Meanwhile, MPR can occur through the sequential emission of three phonons, which is necessary to bridge the $^5D_1$−$^5D_0$ energy difference (considering the 580 cm^{-1} phonon energy of the host material). The dominant relaxation mechanism remains an intriguing question. One should be aware that CR processes are generally related to MPR, where a higher MPR increases CR.[51,52] Therefore, both mechanisms are closely linked, and focusing on MPR may provide valuable insights into non-Boltzmann characteristics.

For the studied system, the $^5D_1 \rightarrow {}^5D_0$ MPR process is 2 orders of magnitude greater than the multiphonon absorption, i.e., MPA ($^5D_1 \leftarrow {}^5D_0$), as shown in Figure S16. Further details on the methodology used to obtain these rates are summarized in the multiphonon relaxation section of Note S2. This implies that, as expected, the population of the $^5D_1$ manifold decreases substantially with increasing temperature. Given that excitation occurs directly at the $^5D_2$ level, analyzing the dynamics of this state is crucial. Accordingly, the $^5D_2 \rightarrow {}^5D_1$ MPR is faster compared to the $^5D_2 \rightarrow {}^5D_0$ (Figure S17), indicating competition between population and depopulation at the $^5D_1$ level. One should also consider the radiative decay at the $^5D_1$ state, which introduces an additional pathway to diminish the $^5D_1$ population. To detail the non-Boltzmann behavior, all pathways should be examined (Figures 3c and S15−S19), leading to a system of ordinary differential equations (ODEs) summarized in Note S5 and eq S29. The population analysis of the $^5D_1/^5D_0$ thermally coupled pair, shown in Figure S20, reveals a two-order magnitude difference between $^5D_0$ (10^{-5}) and $^5D_1$ (10^{-7}), suggesting that the $^5D_1 \rightarrow {}^5D_0$ MPR indeed dominated over other pathways. This finding is consistent with the experimental non-Boltzmann behavior observed between the TCLs. This quantitative output opens an avenue for designing novel luminescent thermometers by finely tuning nonradiative phenomena within a system which has not been previously investigated in the literature.

Following the conventional route of guesswork to select thermometric parameters, the ratiometric approach, i.e., the ratio between R_{02} and R_{1J} in Figure 3a, was fitted to a sigmoidal decay logistic function, while the thermal dependence of the $^5D_0$ lifetime was fitted with an exponential decay function. These fits were employed to calculate the relative thermal sensitivity (S_r) and temperature uncertainty (δT), as depicted in Figure 3d,e. For further details on the thermometric

Downloaded from pubs.acs.org/cmatex/article-pdf/37/9/3125/4118176/cm4c03173.pdf by UNIV ESTADUAL PAULISTA user on 05 November 2026

https://doi.org/10.1021/acs.chemmater.4c03173
Chem. Mater. 2025, 37, 3125−3136

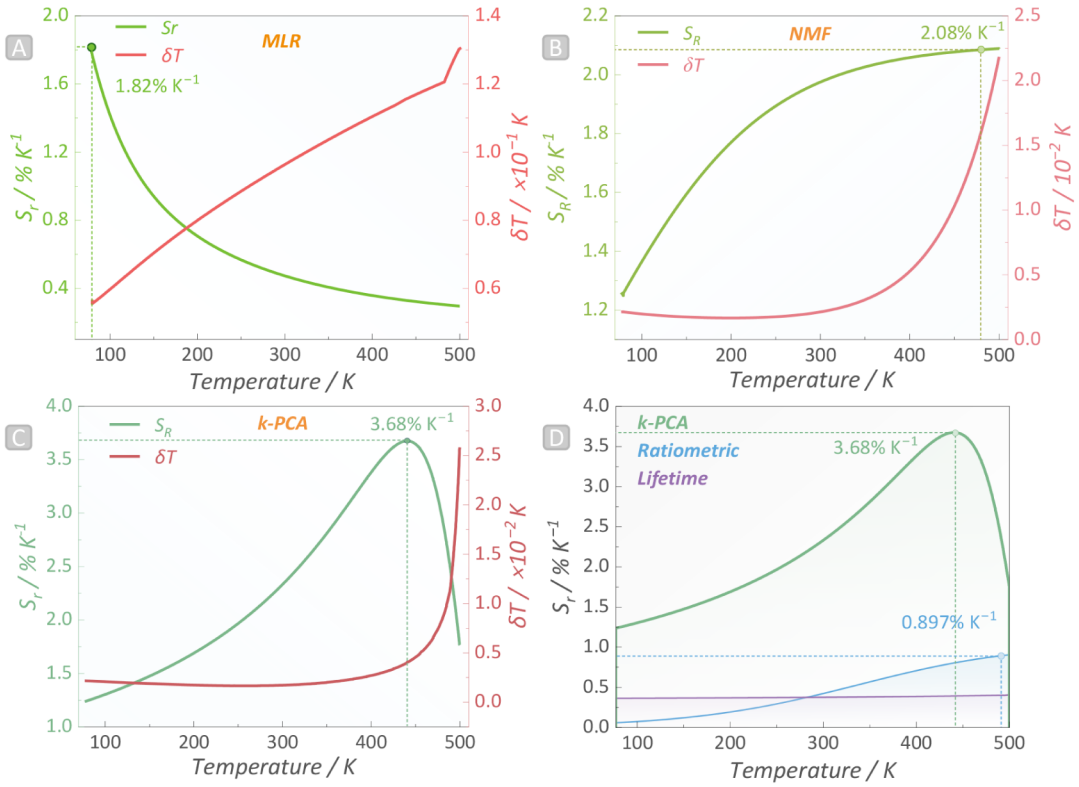


Figure 4. Relative thermal sensitivities (S_r) and temperature uncertainty (δT) obtained using (a) MLR, (b) NMF, and (c) kernel-PCA dimensionality reduction methods. (d) Performance of the k-PCA approach compared to single-parametric thermometry in terms of relative sensitivity. A full comparison is shown in Figure S22 for S_r and Figure S23 for δT.

analyses, please refer to Note S1. In both cases, maximum relative sensitivities of 0.897% K^{-1} and 0.402% K^{-1} were observed for the ratiometric and lifetime methods, respectively, near 500 K. These sensitivities fall below the typical value of 1% K^{-1} generally observed in ratiometric thermometry using TCLs. However, they exhibit low thermal uncertainty due to the high signal-to-noise ratio in the emission spectra. Accordingly, adjusting the parameters to maximize the signal-to-noise ratio combined with an appropriate temperature control is indispensable for the performance of LThs.[53] The same trend pertains to the lifetime measurements; although S_r assumed low values, an even lower δT was noticed at the same optimal temperature. Therefore, searching for a specific thermometric parameter proves insufficient to harness the full potential of our luminescent thermometer, as it may not always yield better thermal readouts.

Dimensionality Reduction Luminescence Thermometry. At first glance, merging different parameters to mitigate bias in selecting the most suitable thermometric parameter may seem unphysical. However, this approach captures equivalent temperature dependencies across distinct spectroscopic properties, resulting in a unified parameter that is most sensitive to thermal changes. This scenario can be accomplished using dimensionality reduction (DR) techniques. In this context, a brief revisit of how DR methods proceed is crucial, along with a summary of applicable approaches. As discussed by Ximendes *et al.*,[31] DR methods typically involve transforming input data into correlations of variables that share similar dependencies. Such transformation can proceed through either linear or nonlinear combinations of the original variables, leading to the linear and nonlinear categories of DR methods.

Among the linear category, principal component analysis (PCA),[54] multiple linear regression (MLR),[27] and multidimensional scaling (MDS)[55] are prominent examples. In contrast, kernel-PCA (k-PCA),[39] non-negative matrix factorization (NMF),[56] and local linear embedding (LLE)[57] represent classical examples of nonlinear DR methods. For our thermometer, MLR, NMF, and k-PCA were the focal points because they encompass both classes while operating well in the absence of a high density of data points. This characteristic is advantageous for most thermometric essays, where high data-point density is typically achieved only by successive measurements with very small temperature increments (<0.1 K, for example). Consequently, using a DR method that heavily relies on data point density could yield erroneous values due to misleading projection of the data set onto lower-dimensional space.[31]

As shown in Figure 3d, both single parameters (Δ and τ) exhibit nonlinear temperature dependence. Thus, to employ MLR without compromising performance, it is necessary to linearize the input variables using eq S22. The calculated temperatures for each parameter, as determined by the thermometer calibration, showed a desired agreement with the measured temperatures (Figure S21), maintaining an almost 1:1 relationship. This result allowed us to proceed with MLR by indirectly considering the thermometric parameter as the newly calculated temperature. Notably, this method resulted in a 2-fold increase in sensitivity (Figure 4a), with a change in the S_r profile, compared to the conventional approach. This modification stems from the linearization step, whereas the input variables are reorganized due to the calibration of the thermometer. Concomitantly, the temperature uncertainty (δT) was comparable to that obtained from

https://doi.org/10.1021/acs.chemmater.4c03173
Chem. Mater. 2025, 37, 3125−3136

Downloaded from pubs.acs.org/cmatex/article-pdf/37/9/3125/4187176/cm4c03173.pdf by UNIV ESTADUAL PAULISTA user on 05 November 2026

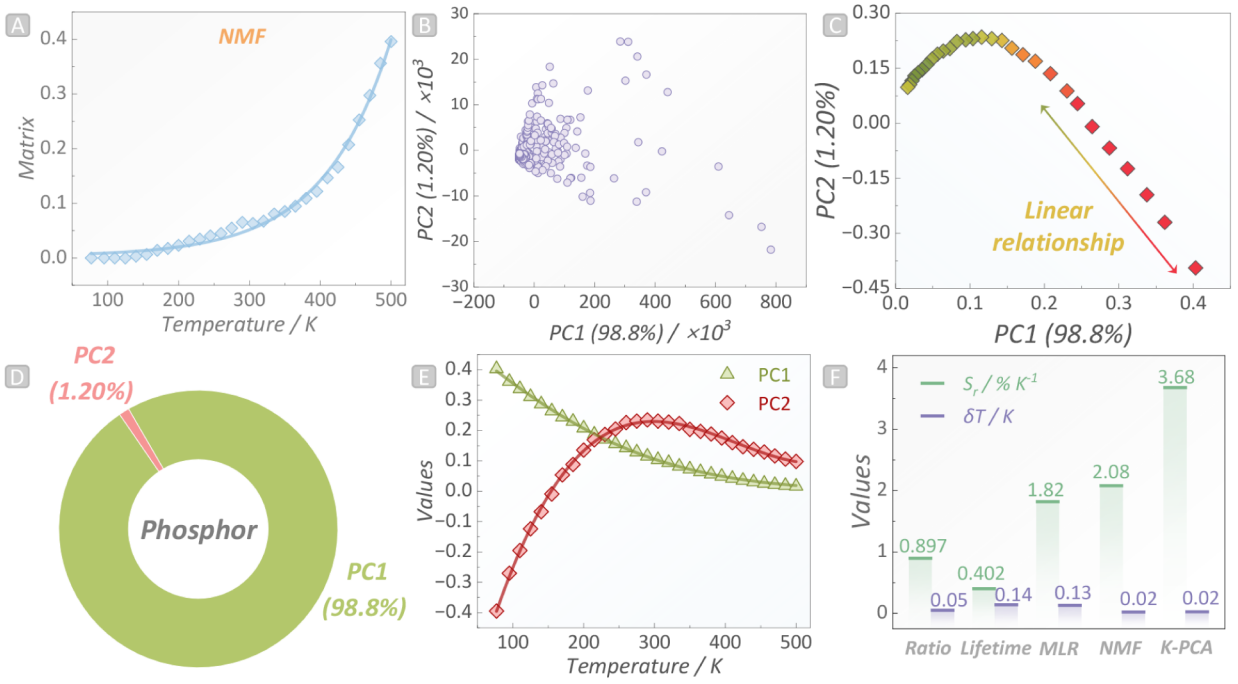


Figure 5. (a) NMF-factored matrix dependence on temperature. (b) Scores plot between the variables of principal component 1 (PC1) and principal component 2 (PC2). (c) Correlation between PC1 and PC2. (d) Donut chart showing the contribution of PC1 and PC2 to reduced data. (e) Thermal dependence of both principal components, where only PC1 was used to estimate the figure of merits. (f) Comparison of maximum relative sensitivity and thermal uncertainty obtained from each single- and dual-parametric approach. These values were obtained at temperatures of 495 K (S_r and δT) for the ratiometric, 500 K (S_r) and 77 K (δT) for the lifetime, 77 K (S_r) and 500 K (δT) for the MLR, 480 K (S_r) and 500 K (δT) for the NMR, 440 K (S_r) and 500 K (δT) for the k-PCA approaches.

the thermal dependence of lifetime (Figure 3f). Such behavior is directly related to the contributions of the parameters (Figure S21c), where the ratiometric was the primary one (96%) compared to the lifetime (only 4%). It should be noted that the sensitivity gain was not as high as that reported by Maturi *et al.*,[27] which may be attached to the different thermal dependencies of the parameters and the inclusion of the linearization step preceding the regression. Ensuring correct linearization is the key for MLR, as this is the main source of errors in the method, potentially crippling the outcomes of this algorithm. In this sense, to improve this method, one could consider using additional variables to predict the thermal readout; otherwise, the MLR would render the same result as a classical linear regression. Additionally, selecting only a portion of the temperature range that displays a linear thermal dependence could avoid the need for linearization, potentially enhancing the approach.

Although the initial protocol emphasized the ability of DR to harvest higher sensitivities, it also made clear that relying solely on linear approaches could limit the effectiveness of the proposed thermometer. This noteworthy observation directs our attention toward nonlinear DR. Within this framework, by preprocessing the collected data (for more information, please refer to the experimental section and Note S3), the NMF algorithm was directly employed. This method uncovers patterns hidden among the input variables by decomposing the matrix containing all thermometric data into two smaller non-negative matrices. Generally, one of these matrices captures the patterns extracted from the original matrix (basis vectors), while the other contains the coefficients needed to reconstruct the original input (spectral profile). A detailed account of the NMF is provided in Note S3, along with relevant references.[56,58] It is worth mentioning that due to the non-negative nature of the factored matrix, it does not cross the zero boundary at any temperature (Figure 5a). This property facilitates the direct computation of S_r values, which otherwise could lead to indetermined sensitivity at a critical temperature and consequently mislead thermal readouts. Using this approach, an even higher enhancement in the S_r (2.3-fold increase) was achieved (Figure 4b). In contrast to MLR, the S_r profile approaches the ones obtained by the conventional analysis, which is attached to the decomposition of the original input from the basis vectors. However, the main advantage of employing NMF over MLR lies in the temperature uncertainty, where the observed values were below 0.03 K. The extremely low uncertainty highlights the potential of this method, particularly in fields where high thermal resolution is critical. This scenario is often seen in the biomedical field, where many physiological processes involve temperature changes in the range of 0.1−1 °C.[59]

Despite this promising outcome, factoring the input matrix may yield two or more patterns of thermal dependencies, raising the question of which pattern to use, representing a significant challenge. Smaller data sets, for instance, contain less information on thermal behavior, resulting in sparse dependence. In such cases, extracting a consistent single pattern from the data points becomes increasingly difficult, potentially leading to several patterns with an illogical nature. This can be seen as a consequence of the local minima problem, which affects the numerical optimization by different starting points, which can be circumvented by multiple normalization of the data set,[56] however, different patterns are still possible. This situation complicates the evaluation of the thermometer performance, as different patterns may

https://doi.org/10.1021/acs.chemmater.4c03173
Chem. Mater. 2025, 37, 3125−3136

Downloaded from pubs.acs.org/cmatex/article-pdf/37/9/3125/4187176/cm4c03173.pdf by UNIV ESTADUAL PAULISTA user on 05 November 2026

exhibit variations in performance across different segments of the employed temperature range. Regardless of these disadvantages, this method still outperformed conventional MLR in this essay and has not yet been reported in the context of luminescence thermometry. Hence, it represents a notable advancement for treating thermometric data to harness the hidden potential of luminescent thermometers.

In an attempt to circumvent the limitations of the previous methods, kernel principal component analysis (*kernel*-PCA or k-PCA) was also applied to the proposed system. The procedure for employing this algorithm is thoroughly described in Note S3, and a more in-depth discussion of k-PCA is available in reference.[39] In classical PCA, the data points form a *p*-dimensional ellipsoid, where new axes (directions) are identified to capture the most variation.[31] However, this approach only identifies linear directions and fails to properly harness nonlinear dependencies. By incorporating the *kernel* trick, nonlinear relationships can be transformed into linear ones, thereby allowing standard PCA treatment.[35] In this context, careful attention must be paid to the kernel function, which defines how data are transformed. As mentioned earlier; to facilitate the evaluation of thermal sensitivity, the output data must not cross the zero boundary. Therefore, an exponential *kernel* function was constructed to measure the similarity between two data points using an exponential function (Note S6).

By employing k-PCA on the system under study, two principal components (PC1 and PC2) were identified, and a reasonable correlation was observed between them (Figure 5b,c). However, the scattering of data points along the first principal component at null scores of PC2 indicates that PC1 holds the major contribution (98.8%), as represented by the donut chart in Figure 5d. This result allows us to primarily rely on PC1 to study thermal dependence. To this end, understanding the behavior of PC1 with temperature is crucial. PC1 retained the original exponential decay behavior of the employed kernel function with only positive values (Figure 5e). Consequently, using PC1 as the new unified thermometric parameter rendered a maximum thermal sensitivity (Figure 4c) of 3.68% K^{-1}, representing a 4.1-fold increase (Figure 4d), while maintaining thermal uncertainty below 0.03 K. These low uncertainty values are comparable to those obtained through the NMF approach while avoiding the possibility of identifying multiple patterns among the input variables. This remarkable outcome demonstrates the potential of k-PCA for luminescence thermometry because it excels at capturing nonlinear relationships, allowing for higher sensitivities with minimal impact on thermal resolution. It should be noted that if only linear dependencies are present, a standard PCA algorithm is suitable for treating the data.[31] However, standard PCA does not use *kernel* functions, meaning that the principal component can easily cross the zero boundary, making it infeasible to evaluate thermal sensitivity.

At this point in the discussion, it is pertinent to summarize the performance of all employed methods. As illustrated in Figure 5f, all the dual-parametric DR approaches outperform the single-parametric ones. This improvement is attached to the inclusion of relationships between data points that are typically concealed in classical thermometric analyses. Among the considered methods, the k-PCA approach demonstrated the highest increase in performance, as shown in Figure 5f. The main reason for this observation is not entirely clear; however, two main hypotheses can be proposed: (*i*) the aggregation of multiple subtle thermal dependencies into a single component, and (*ii*) the use of a finely tuned *kernel* function that enables accurate data projection. It is also noteworthy that both NMF and k-PCA reduced the maximum thermal uncertainty to unprecedented values. Given these discussions, the outstanding findings of this study indeed hold potential for the spotlight of luminescence thermometry. Meanwhile, a wide range of DR methods remain available, suggesting that more sophisticated machine learning algorithms for luminescence thermometry can be constructed in future studies combining more parameters or different thermometric approaches.

CONCLUSION

In summary, this study provides a thorough demonstration of how different dimensionality reduction (DR) methods can boost the performance of luminescent thermometers by effectively handling and analyzing data sets. Using SrY_2O_4:$Tb^{III/IV}$,Eu^{III} phosphor as proof-of-concept, the investigation revealed how integrating multiple thermometric parameters can significantly improve thermal sensing capabilities. The synergy between the structural and optical properties validated the feasibility of the selected phosphor, as emission bands assigned to the $^5D_1$ level were observed in addition to the common set of $^5D_0 \rightarrow {}^7F_{0-4}$ Eu^{III} transitions. By employing the ratio of these emission bands ($^5D_1 \rightarrow {}^7F_J$ and $^5D_0 \rightarrow {}^7F_2$), a non-Boltzmann profile of the thermometer was identified despite the thermally coupled nature of these excited levels, which was primarily driven by multiphonon relaxation processes. Under the lifetime regime, a similar behavior was observed, with both maximum sensitivities operating within the same temperature interval. Consequently, applying DR to the combined data set improved the thermal response by enhancing sensitivity and reducing the uncertainty to unprecedented values. Specifically, k-PCA excelled among the DR methods, fostering a 4.1-fold enhancement of thermal sensitivity (3.68% K^{-1}) compared to the ratiometric approach (0.897% K^{-1}). This interesting outcome unfolds how advancing postprocessing data methodologies can significantly boost the capabilities of luminescent thermometers, rather than solely relying on material development. Therefore, it sets the stage for using DR methods to treat multiple parameters and demonstrates its potential to harness the hidden performance of a simple system. The future of these algorithms in luminescence thermometry is promising, and new implementations are likely to drive exciting developments in this field.

METHODS

Materials. Rare earth oxides (RE_2O_3, RE = Y^{III}, Tb^{III}, Eu^{III}, ≥ 99.9%), strontium carbonate ($SrCO_3$, 99.99%), nitric acid (HNO_3, 70%), ethylenediaminetetraacetic disodium salt dihydrate ($Na_2EDTA{\cdot}2H_2O$, 99.0%), citric acid (CA, 99.5%), and sorbitol (SB, 99.0%) were purchased from Sigma-Aldrich and used without further purification.

Synthesis. SrY_2O_4:$Tb^{III/IV}$,Eu^{III} powder samples were synthesized based on a previous adaptation of the Pechini method.[37,60] $Sr(NO_3)_2$ and $RE(NO_3)_3$ (RE = Y^{III}, Eu^{III}, Tb^{III}) precursors were used aiming Eu^{III} and Tb^{III} ions to replace Y^{III} sites in the matrix. Rare earth and strontium nitrates were prepared by reacting RE_2O_3 and $SrCO_3$ with nitric acid (HNO_3, 1 mol L^{-1}), while the exact concentration was determined from a complexometric titration with $Na_2EDTA{\cdot}2H_2O$ with xylenol orange as indicator. The aqueous solution

Downloaded from pubs.acs.org/cmatex/article-pdf/37/9/3125/4118717/cm4c03173.pdf by UNIV ESTADUAL PAULISTA user on 05 November 2026

https://doi.org/10.1021/acs.chemmater.4c03173
Chem. Mater. 2025, 37, 3125−3136

containing the metal precursors at the desired stoichiometric proportion was heated at 80 °C under magnetic stirring followed by the addition of CA and SB at the following proportions: CA:Metal = 1:2 and SB:Metal = 1:1 (mol:mol). After solvent evaporation, a yellowish polymeric resin was accomplished, which was fired in furnace at 350 °C for 3 h upon air atmosphere, yielding the precursor charcoal. The charcoal was further deagglomerated in a 325-mesh sieve and annealed in a furnace at 1100 °C for 5 h (heating ramp of 10 °C min^{-1}), resulting in a yellow powder. The Tb^{III} doping concentration was fixed at 2 at.% while the Eu^{III} amount was varied in odd concentrations (3−9 at.%), yielding the following samples: SrY_2O_4:$Tb^{III/IV}$(2 at.%),Eu^{III}(3, 5, 7, or 9 at.%). All the structural and optical characterizations of the materials are thoroughly described in Note S1. The theoretical and computational modeling procedure is detailed in Note S2.

Photoluminescence Thermometry Data Preprocessing for Dimensionality Reduction. To analyze the photoluminescence thermometry data via dimensionality reduction, a set of preprocessing steps were taken. These steps follow the ones mentioned by Ximendes, Marin and coworkers[31] with a few slight modifications regarding each algorithm. First, the values of intensity corresponding to the wavelengths in which no significant signal had been observed were manually removed. Accordingly, only the wavelengths corresponding to transitions between $^5D_1 \rightarrow {}^7F_{0-2}$ and $^5D_0 \rightarrow {}^7F_2$ were maintained. All corresponding spectra were normalized and then mean-centered. Subsequently, they were stored in a matrix consisting of 29 rows (number of temperature points, i.e., 77−500 K with an increment of 15 K starting from 95 K) and 184 columns (number of wavelengths in which the intensity was measured). The columns of this matrix were renormalized using the standard normal variation (SNV) procedure. A second matrix was created using the lifetime consisting of the same 29 rows and 2048 columns, consisting of the time when the photon counting was non-null. This second matrix was also SNV normalized, and the two matrices were joined and set as the input data in the dimensionality reduction (DR) models. For abbreviation, this matrix will be referred to as $\boldsymbol{K}^{std}$.

Kernel-PCA. This method extends traditional principal component analysis (PCA) by first mapping the original *p*-correlated variables into a higher-dimensional *kernel* space to capture nonlinear relationships. In summary, the procedure starts with the computation of a covariance matrix in the *kernel* space, where the entries are derived from standardized *kernel* values across the data set. An eigen-decomposition is then performed on this covariance matrix to obtain its eigenvalues and corresponding eigenvectors. These eigenvectors are arranged in descending order of their eigenvalues, aligning them with the degree of variance captured from the original data.[31] Subsequently, the standardized temperature-dependent data are projected onto these sorted eigenvectors through the reproducing *kernel* Hilbert space, whose analytical form of the transformation is not explicitly known, but interpreted as a correction factor for the projection, allowing the retrieval of the principal components (PCs) with the most variance. With these results, these PC projections were analyzed to explore their temperature dependencies, enabling them to recover relative sensitivity. For more information regarding the algorithm and the steps, proceed to the kernel-PCA section of Note S3—Data analysis methodology for luminescence thermometry.

Non-Negative Matrix Factorization (NMF). In contrast to k-PCA, NMF approaches the data by approximating the original data matrix $\boldsymbol{K}^{std}$ as a product of two lower-dimensional matrices, $\boldsymbol{W}$ and $\boldsymbol{H}$, whose elements are constrained to be non-negative. In this framework, $\boldsymbol{H}$ captures the basis vectors, essentially representing the characteristic emission and lifetime patterns observed at different temperatures, while $\boldsymbol{W}$ contains the weights that quantify the contribution of each basis vector across the temperature range. In this sense, the rows of $\boldsymbol{H}$ represent the variation index across all temperatures (29 rows in this case), allowing us to retrieve the relative sensitivity. The factorization of the original matrix $\boldsymbol{K}^{std}$ was conducted by minimizing the reconstruction error, defined as the Frobenius norm of the difference between K^{std} and $\boldsymbol{WH}$, i.e., $min_{W,H}\|K^{std} - WH\|_F^2$. After the optimization, a set of data from matrix $\boldsymbol{H}$ was fitted to an exponential growth function, where the relative sensitivity was then calculated. For more information regarding the algorithm, refer to the non-negative matrix factorization section of Note S3—Data analysis methodology for luminescence thermometry.

Multiple Linear Regression (MLR). In contrast to k-PCA and NMF, multiple linear regression (MLR) is a linear dimensionality reduction procedure that was employed to model the relationship between the measured spectroscopic parameters and the final temperature.[27] Recognizing that the parameters (such as the ratiometric and lifetime in this case) often exhibit nonlinear dependencies on temperature, a transformation is first applied to linearize these relationships.[29] For instance, the lifetime data are transformed using an exponential decay model (eq S22a), and the ratiometric data are linearized through a sigmoidal logistic function (eq S22b). These transformations yield new temperature-related variables that were then used as independent predictors in a linear regression model. The model expresses the final temperature as a linear function of these transformed variables, with regression coefficients (β_i) quantifying the sensitivity of the temperature to each parameter. In this model, the final temperature would be the corresponding vector in the *z*-axis, allowing us to recast the relative sensitivity using eq 1. For more information regarding the algorithm, proceed to the MLR section of Note S3—Data analysis methodology for luminescence thermometry.

$$S_r = \sqrt{\sum_i (\beta_i T_i)^{-2}} \tag{1}$$

■ ASSOCIATED CONTENT

Supporting Information

The Supporting Information is available free of charge at https://pubs.acs.org/doi/10.1021/acs.chemmater.4c03173.

Detailed preparation and characterization procedures, advanced structural studies including theoretical simulations, and data analysis procedures and implementations (PDF)

■ AUTHOR INFORMATION

Corresponding Authors

Ana M. Pires − *Department of Chemistry and Biochemistry, School of Sciences and Technology, São Paulo State University (UNESP), Presidente Prudente 19060-900, Brazil; Institute of Biosciences, Humanities and Exact*

https://doi.org/10.1021/acs.chemmater.4c03173
Chem. Mater. 2025, 37, 3125−3136

Downloaded from pubs.acs.org/cmatex/article-pdf/37/9/3125/4118176/cm4c03173.pdf by UNIV ESTADUAL PAULISTA user on 05 November 2026

Sciences, São Paulo State University (UNESP), São José do Rio Preto 15054-000, Brazil; Email: ana.maria@unesp.br

Airton G. Bispo-Jr. − *Institute of Chemistry, University of São Paulo (USP), São Paulo 05508-900, Brazil*; Email: airton.bispo.junior@iq.usp.br

Fernando A. Sigoli − *Institute of Chemistry, University of Campinas (UNICAMP), Campinas 13083-970, Brazil*; Email: fsigoli@unicamp.br

Authors

Leonardo F. Saraiva − *Department of Chemistry and Biochemistry, School of Sciences and Technology, São Paulo State University (UNESP), Presidente Prudente 19060-900, Brazil; Institute of Biosciences, Humanities and Exact Sciences, São Paulo State University (UNESP), São José do Rio Preto 15054-000, Brazil;* orcid.org/0000-0002-1963-9854

André L. Costa − *Department of Chemistry and Biochemistry, School of Sciences and Technology, São Paulo State University (UNESP), Presidente Prudente 19060-900, Brazil; Institute of Biosciences, Humanities and Exact Sciences, São Paulo State University (UNESP), São José do Rio Preto 15054-000, Brazil*

Sergio A. M. Lima − *Department of Chemistry and Biochemistry, School of Sciences and Technology, São Paulo State University (UNESP), Presidente Prudente 19060-900, Brazil; Institute of Biosciences, Humanities and Exact Sciences, São Paulo State University (UNESP), São José do Rio Preto 15054-000, Brazil*

Complete contact information is available at: https://pubs.acs.org/10.1021/acs.chemmater.4c03173

Author Contributions

L.F.S.: term, conceptualization, methodology, validation, formal analysis, investigation, theoretical calculations, algorithms, data curation, writing − original draft; A.G.B.Jr.: formal analysis, investigation, writing − original draft; A.L.C.: methodology, formal analysis; F.A.S.: term, methodology, resources, writing − review and editing; S.A.M.L.: term, methodology, resources, writing − review and editing; A.M.P.: term, conceptualization, methodology, resources, writing − review and editing, supervision, project administration.

Funding

The Article Processing Charge for the publication of this research was funded by the Coordenacao de Aperfeicoamento de Pessoal de Nivel Superior (CAPES), Brazil (ROR identifier: 00x0ma614).

Notes

The authors declare no competing financial interest.

■ ACKNOWLEDGMENTS

The authors are thankful to all funding agencies that supported this research, FAPESP 2023/05718-9 and CNPq 309448/2021-2, and the computations supplied by the Center of Scientific Computing (NCC/GridUnesp) no. 137 of São Paulo State University. The authors are also thankful to the Group of Nanomaterials and Advanced Ceramics (Institute of Physics, University of São Paulo) for the XPS measurements, Laboratory of Nanostructure Films and Spectroscopy (FCT-UNESP) for the Raman spectroscopy measurements, Ceramic Materials Laboratory (FCT-UNESP) for the XRD measurements and the Multiuser Laboratory of Advanced Optical Spectroscopy (LISPEC) of the Institute of Chemistry-UNICAMP. ALC thanks CAPES 88887.686388/2022-00. F.A.S. thanks FAPESP (2021/06326-1 and 2021/08111-2) and CNPq (304807/2022-2). SAML thanks CNPq: 308868/2022-6.

■ REFERENCES

(1) Heisenberg, W. *Physics and Philosophy: The Revolution in Modern Science*; Harper & Row: New York, 1958.

(2) Brites, C. D. S.; Marin, R.; Suta, M.; Carneiro Neto, A. N.; Ximendes, E.; Jaque, D.; Carlos, L. D. Spotlight on Luminescence Thermometry: Basics, Challenges, and Cutting-Edge Applications. *Adv. Mater.* **2023**, *35*, 2302749.

(3) Bednarkiewicz, A.; Marciniak, L.; Carlos, L. D.; Jaque, D. Standardizing luminescence nanothermometry for biomedical applications. *Nanoscale* **2020**, *12*, 14405−14421.

(4) Zhou, J.; Del Rosal, B.; Jaque, D.; Uchiyama, S.; Jin, D. Advances and Challenges for fluorescence nanothermometry. *Nat. Methods* **2020**, *17*, 967−980.

(5) Far, L. D.; Dramicanin, M. D. Luminescence Thermometry with Nanoparticles: A Review. *Nanomaterials* **2023**, *13*, 2904.

(6) Ćirić, A.; Gavrilovic, T. G.; Dramicanin, M. D. Luminescence Intensity Ratio Thermometry with Er^{3+}: Performance Overview. *Crystals* **2021**, *11*, 189.

(7) Suta, M.; Meijerink, A. A Theoretical Framework for Ratiometric Single Ion Luminescent Thermometers—Thermodynamic and Kinetic Guidelines for Optimized Performance. *Adv. Theory Simul.* **2020**, *3*, 2000176.

(8) Mendez-Gonzalez, D.; Lifante, J.; Gutierrez, I. Z.; Marin, R.; Ximendes, E.; Sanz-de Diego, E.; Iglesias-de-la Cruz, M. C.; Teran, F. J.; Rubio-Retama, J.; Jaque, D. Optomagnetic nanofluids for controlled brain hyperthermia: A critical study. *Nanoscale* **2022**, *14*, 16208−16219.

(9) Shen, Y.; Santos, H. D. A.; Ximendes, E. C.; Lifante, J.; Sanz-Portilla, A.; Monge, L.; Fernández, N.; Chaves-Coira, I.; Jacinto, C.; Brites, C. D. S.; et al. Ag_2S Nanoheaters with Multiparameter Sensing for Reliable Thermal Feedback during In Vivo Tumor Therapy. *Adv. Funct. Mater.* **2020**, *30*, 2002730.

(10) Gu, Y.; Piñol, R.; Moreno-Loshuertos, R.; Brites, C. D. S.; Zeler, J.; Martínez, A.; Maurin-Pasturel, G.; Fernández-Silva, P.; Marco-Brualla, J.; Téllez, P.; et al. Local Temperature Increments and Induced Cell Death in Intracellular Magnetic Hyperthermia. *ACS Nano* **2023**, *17* (7), 6822−6832.

(11) Terlingen, B. J. P.; Arens, T.; Van Swieten, T. P.; Rabouw, F. T.; Prins, P. T.; de Beer, M. M.; Meijerink, A.; Ahr, M. P.; Hutter, E. M.; van Lare, C. E. J.; et al. Bifunctional Europium for Operando Catalyst Thermometry in an Exothermic Chemical Reaction. *Angew. Chem., Int. Ed.* **2022**, *61* (52), No. e200011991.

(12) Jacobs, T. S.; Van Swieten, T. P.; Vonk, S. J. W.; Bosman, I. P.; Melcherts, A. E. M.; Janssen, B. C.; Janssens, J. C. L.; Monai, M.; Meijerink, A.; Rabouw, F. T.; et al. Mapping Temperature Heterogeneities during Catalytic CO_2 Methanation with Operando Luminescence Thermometry. *ACS Nano* **2023**, *17* (20), 20053−20061.

(13) Bezkrovnyi, O.; Szymczak, M.; Marciniak, L.; Kraszkiewicz, P.; Boiko, V.; Vorochta, M.; Matolinová, I.; Kepinski, L. Eu^{3+} Species as aLuminescent Probe for Fast Monitoring of the Chemical State of Ceria Catalysis. *J. Phys. Chem. C* **2024**, *128* (25), 10465−10473.

(14) Marciniak, L.; Kniec, K.; Elzbieciak-Piecka, K.; Trejgis, K.; Stefanska, J.; Dramicanin, M. Luminescence thermometry with transition metal ions. A review. *Coord. Chem. Rev.* **2022**, *469*, 214671.

(15) Rodríguez-Sevilla, P.; Marin, R.; Ximendes, E.; Del Rosal, B.; Benayas, A.; Jaque, D. Luminescence Thermometry for Brain Activity Monitoring: A Perspective. *Front. Chem.* **2022**, *10*, 941861.

(16) Shen, Y.; Lifante, J.; Zabala-Gutierrez, I.; de la Fuente-Fernández, M.; Granado, M.; Fernández, N.; Rubio-Retama, J.; Jaque, D.; Marin, R.; Ximendes, E.; et al. Reliable and Remote Monitoring of Absolute Temperature during Liver Inflammation via Luminescence-

Downloaded from pubs.acs.org/cmatex/article-pdf/37/9/3125/4118176/cm4c03173.pdf by UNIV ESTADUAL PAULISTA user on 05 November 2026

Lifetime-Based Nanothermometry. *Adv. Mater.* **2022**, *34* (7), 2107764.
(17) Trejgis, K.; Bednarkiewicz, A.; Marciniak, L. Engineering excited state absorption based nanothermometry for temperature sensing and imaging. *Nanoscale* **2020**, *12*, 4667−4675.
(18) Gálico, D. A.; Murugesu, M. Boosting the sensitivity with time-gated luminescence thermometry using a nanosized molecular cluster aggregate. *Nanoscale* **2023**, *15*, 5778−5785.
(19) Szymczak, M.; Mauri, A.; Galli, S.; Marciniak, L.; Fandzloch, M. Highly Sensitive, Multiparametric Thermal History Phosphor Based on An Eu(BTC) Architecture. *Adv. Funct. Mater.* **2024**, *34* (19), 2313045.
(20) Gálico, D. A.; Murugesu, M. Toward Magneto-Optical Cryogenic Thermometers with High Sensitivity: A Magnetic Circular Dichroism Based Thermometric Approach. *Angew. Chem., Int. Ed.* **2023**, *62*, No. e202309152.
(21) Zhao, Z.; Dai, M.; Li, K.; Liang, G.; Wei, Y.; Fu, Z. Towards ultra-sensitive multimodal luminescent thermometers enabled by high crystal field strength of $Lu_2CaMg_2Ge_3O_{12}$: Yb^{3+},Nd^{3+},Er^{3+} phosphors. *Inorg. Chem. Front.* **2024**, *11*, 7955−7965.
(22) Schäfer, S.; Kaufmann, S.; Rösch, E. S.; Roesky, P. W. Divalent metallocenes of the lanthanides − a guideline to properties and reactivity. *Chem. Soc. Rev.* **2023**, *52*, 4006−4045.
(23) Serna-Gallén, P.; Beltrán-Mir, H.; Cordoncillo, E. Practical guidance for easily interpreting the emission and physicochemical parameters of Eu^{3+} in solid-state hosts. *Ceram. Int* **2023**, *49*, 41078−41089.
(24) Thor, W.; Bünzli, J.-C. G.; Wong, K.-L.; Tanner, P. A. Shedding Light on Luminescence Lifetime Measurement and Associated Data Treatment. *Adv. Photonics Res.* **2025**, *6*, 2400081.
(25) Ciric, A.; Marciniak, Ł.; Dramicanin, M. D. Luminescence intensity ratio squared—A new luminescence thermometry method for enhanced sensitivity. *J. Appl. Phys.* **2022**, *131*, 114501.
(26) Ge, X.; Fu, Z. Multiwavelength Responsive Luminescence for Temperature Sensing and Visualized Information Encoding/Decoding Based on Er^{3+}/Tb^{3+}-Doped $Ba_2Ga_2GeO_7$ Phosphors. *ACS Sustainable Chem. Eng.* **2023**, *11* (16), 6362−6372.
(27) Maturi, F. E.; Brites, C. D. S.; Ximendes, E. C.; Mills, C.; Olsen, B.; Jaque, D.; Ribeiro, S. J. L.; Carlos, L. D. Going Above and Beyond: A Tenfold Gain in the Performance of Luminescence Thermometers Joining Multiparametric Sensing and Multiple Regression. *Laser Photonics Rev.* **2021**, *15*, 2100301.
(28) Chen, Y.; Li, G.; Ding, Y.; Mao, Q.; Liu, M.; Wang, C.; Zheng, R.; Su, B.-L.; Zhong, J. Antithermal Quenching and Multiparametric Temperature Sensing from Mn^{2+}/Tb^{3+}-Codoped Ca_2LaTaO_6 Phosphor. *Adv. Photonics Res.* **2023**, *4* (6), 2300106.
(29) Alrebdi, T. A.; Alodhayb, A. N.; Ristic, Z.; Dramicanin, M. D. Comparison of Performance between Single- and Multiparameter Luminescence Thermometry Based on the Mn^{5+} Near-Infrared Emission. *Sensors* **2023**, *23*, 3839.
(30) Ortiz-Rivero, E.; Prorok, K.; Marin, R.; Bednarkiewicz, A.; Jaque, D.; Haro-González, P. Unlocking Single-Particle Multiparametric Sensing: Decoupling Temperature and Viscosity Readouts through Upconverting Polarized Spectroscopy. *Small Methods* **2024**, 2400718.
(31) Ximendes, E.; Marin, R.; Carlos, L. D.; Jaque, D. Less is more: Dimensionality reduction as a general strategy for more precise luminescence thermometry. *Light: Sci. Appl.* **2022**, *11*, 237.
(32) Santos, E. P.; Pugina, R. S.; Hilário, E. G.; Carvalho, A. J. A.; Jacinto, C.; Rego-Filho, F. A. M. G.; Canabarro, A.; Gomes, A. S. L.; Caiut, J. M. A.; Moura, A. L. Towards accurate real-time luminescence thermometry: An automated machine learning approach. *Sens. Actuators, A* **2023**, *362*, 114666.
(33) Ming, L.; Zabala-Gutierrez, I.; Rodríguez-Sevilla, P.; Rubio Retaman, J.; Jaque, D.; Marin, R.; Ximendes, E. Neural Networks Push the Limits of Luminescence Lifetime Nanosensing. *Adv. Mater.* **2023**, *35* (52), 2306606.
(34) Rajčić, A.; Ristić, Z.; Periša, J.; Milićević, B.; Aldawood, S.; Alodhayb, A. N.; Antić, Ž.; Dramićanin, M. D. Using Principal Component Analysis for Temperature Readings from YF_3: Pr^{3+} Luminescence. *Technologies* **2024**, *12* (21), 131.
(35) Velliangri, S.; Alagumuthukrishnan, S.; Iwin Thankumar joseph, S. A Review of Dimensionality Reduction Techniques for Efficient Computation. *Procedia Comp. Sci.* **2019**, *165*, 104−111.
(36) Jia, W.; Sun, M.; Lian, J.; Hou, S. Feature dimensionality reduction: A review. *Complex Intell. Syst.* **2022**, *8*, 2663−2693.
(37) Saraiva, L. F.; Bispo-Jr, J. A. G.; Lima, S. A. M.; Pires, A. M. Eu^{3+}-activated SrY_2O_4: $Ce^{4+/3+}$ red-phosphor for WLEDs: Structural and luminescent insights from experimental and theoretical approaches. *J. Alloys Comp.* **2023**, *938*, 168595.
(38) Geitenbeek, R. G.; de Wijn, H. W.; Meijerink, A. Non-Boltzmann Luminescence in $NaYF_4$: Eu^{3+}: Implications for Luminescence Thermometry. *Phys. Rev. Appl.* **2018**, *10*, 064006.
(39) Marukatat, S. Tutorial on PCA and approximate kernel PCA. *Artif. Intell. Rev.* **2023**, *56*, 5445−5477.
(40) Gálico, D. A.; Rodrigues, E. M.; Halimi, I.; Toivola, J.; Zhao, H.; Xu, J.; Moilanen, J. O.; Liu, X.; Hemmer, E.; Murugesu, M. Confining single Er^{3+} ions in sub-3 nm $NaYF_4$ nanoparticles to induce slow relaxation of the magnetisation. *Nat. Commun* **2024**, *15*, 3498.
(41) Caixeta, F. J.; Bastos, A. R. M.; Botas, A. M. P.; Rosa, L. S.; Souza, V. S.; Borges, F. H.; Carneiro Neto, A. N.; Ferrier, A.; Goldner, P.; Carlos, L. D.; et al. High-Quantum-Yield Upconverting Er^{3+}/Yb^{3+}-Organic−Inorganic Hybrid Dual Coatings for Real-Time Temperature Sensing and Photothermal Conversion. *J. Phys. Chem. C* **2020**, *124* (37), 19892−19903.
(42) Carneiro Neto, A. N.; Moura, R. T., Jr.; Shyichuk, A.; Paterlini, V.; Piccinelli, F.; Bettinelli, M.; Malta, O. L. Theoretical and Experimental Investigation of the Tb^{3+}→Eu^{3+} Energy Transfer Mechanisms in Cubic $A_3Tb_{0.90}Eu_{0.10}(PO_4)_3$ (A = Sr, Ba) Materials. *J. Phys. Chem. C* **2020**, *124* (18), 10105−10116.
(43) Zhong, C.; Xu, Y.; Wu, X.; Ying, S.; Zhang, X.; Zhou, L.; You, H. Near-infrared $Sr_7NaGa(PO_4)_6$: Cr^{3+},Ln^{3+} (Ln = Nd, Er, and Yb) phosphors with different energy transfer paths: Photoluminescence enhancement and versatility. *J. Mater. Chem. C* **2023**, *11*, 3375−3385.
(44) Glorieux, B.; Berjoan, R.; Matecki, M.; Kammouni, A.; Perarnau, D. XPS analyses of lanthanides phosphates. *Appl. Surf. Sci.* **2007**, *253* (6), 3349−3359.
(45) Zhang, X.; Qiu, H.; Luo, W.; Huang, K.; Chen, Y.; Zhang, J.; Wang, B.; Peng, D.; Wang, Y.; Zheng, K. High-Performance X-Ray Imaging using Lanthanide Metal-Organic Frameworks. *Adv. Sci.* **2023**, *10*, No. e2207004.
(46) Marin, R.; Jaque, D.; Benayas, A. Switching to the brighter lane: Pathways to boost the absorption of lanthanide-doped nanoparticles. *Nanoscale Horiz.* **2021**, *6*, 209−230.
(47) Saraiva, L. F.; Bispo-Jr, A. G.; Lima, S. A. M.; Pires, A. M. Unrevealing the opto-structural features of luminescent polymeric films containing Eu^{III}-doped phosphors through spectroscopic and theoretical perspectives. *J. Mater. Chem. C* **2023**, *11*, 14226−14236.
(48) Saraiva, L. F.; Carneiro Neto, A. N.; Bispo-Jr, A. G.; Quintano, M. M.; Kraka, E.; Carlos, L. D.; Lima, S. A. M.; Pires, A. M.; Moura, R. T., Jr. Role of Vibronic Coupling for the Dynamics of Intersystem Crossing in Eu^{3+} Complexes: An Avenue for Brighter Compounds. *J. Chem. Theory Comput.* **2025**, *21* (6), 3066−3076.
(49) Yuan, H.; Zhou, X.; Cao, Y.; Bian, Q.; Zhang, Z.; Sun, H.; Li, S.; Shao, Z.; Hu, J.; Zhu, Y.; et al. Raman detection of hidden phonons assisted by atomic point defects in a two-dimensional semimetal. *npj 2D Mater. Appl.* **2019**, *3*, 12.
(50) Benshalom, N.; Asher, M.; Jouclas, R.; Korobko, R.; Schweicher, G.; Liu, J.; Geerts, Y.; Hellman, O.; Yaffe, O. Phonon-Phonon Interactions in the Polarization Dependence of Raman Scattering. *J. Phys. Chem. C* **2023**, *127* (36), 18099−18106.
(51) Drabik, J.; Kowalski, R.; Marciniak, L. Enhancement of the sensitivity of single band ratiometric luminescent nanothermometers based on Tb^{3+} ions through activation of the cross relaxation process. *Sci. Rep.* **2020**, *10*, 11190.
(52) Huang, F.; Yang, T.; Wang, S.; Lin, L.; Hu, T.; Chen, D. Temperature sensitive cross relaxation between Er^{3+} ions in laminated

Downloaded from pubs.acs.org/cmatex/article-pdf/37/9/3125/4118176/cm4c03173.pdf by UNIV ESTADUAL PAULISTA user on 05 November 2026

hosts: A novel mechanism for thermochromic upconversion and high performance thermometry. *J. Mater. Chem. C* **2018**, *6*, 12364−12370.
(53) Bispo-Jr, A. G.; Saraiva, L. F.; Lima, S. A. M.; Pires, A. M.; Mazali, I. O.; Sigoli, F. A. Lanthanide coordination polymers as luminescent thermometers: Integrating theoretical modeling with experimental analysis to tune the thermal response. *J. Mater. Chem. C* **2025**, *13*, 3320−3330.
(54) Greenacre, M.; Groenen, P. J. F.; Hastie, T.; D'Enza, A. I.; Markos, A.; Tuzhilina, E. Principal Component Analysis. *Nat. Rev. Methods Primers* **2022**, *2*, 100.
(55) Shen, H. T., Multidimensional Scaling In *Özsu, Encyclopedia of Database Systems*. Liu, L.; Özsu, M. T. Eds.; Springer: Boston, MA, 2009.
(56) Lee, D. D.; Sebastian Seung, H. Learning the parts of objects by non-negative matrix factorization. *Nature* **1999**, *401*, 788−791.
(57) Chen, J.; Liu, Y. Locally linear embedding: A survey. *Artif. Intell. Rev.* **2011**, *36*, 29−48.
(58) Wang, Y.-X.; Zhang, Y.-J. Nonnegative Matrix Factorization: A Comprehensive Review. *IEEE Trans. Knowl. Data. Eng.* **2013**, *25* (6), 1336−1353.
(59) Knapp, B. D.; Huang, K. C. The Effects of Temperature on Cellular Physiology. *Annu. Rev. Biophys.* **2022**, *51*, 499−526.
(60) Oliveira, N. A.; Bispo-Jr, G. A. G.; Shinohara, M. M.; Lima, S. A. M.; Pires, A. M. The influence of the complexing agent on the luminescence of multicolor-emitting Y_2O_3: Eu^{3+},Er^{3+},Yb^{3+} phosphors obtained by the Pechini's method. *Mater. Chem. Phys.* **2021**, *257*, 123840.

Downloaded from pubs.acs.org/cmatex/article-pdf/37/9/3125/4118717/cm4c03173.pdf by UNIV ESTADUAL PAULISTA user on 05 November 2026

https://doi.org/10.1021/acs.chemmater.4c03173
Chem. Mater. 2025, 37, 3125−3136